High-speed spatial parameter recovery using multi-distance frequency-domain diffuse optical spectroscopy

Dale, Robin; O'Sullivan, Thomas D.; Howard, Scott; Campbell, Chris; Orihuela-Espina, Felipe; Dehghani, Hamid

DOI:
10.1117/12.2651676

License:
Other (please specify with Rights Statement)

Document Version
Peer reviewed version

Citation for published version (Harvard):
Dale, R, O'Sullivan, TD, Howard, S, Campbell, C, Orihuela-Espina, F & Dehghani, H 2023, High-speed spatial parameter recovery using multi-distance frequency-domain diffuse optical spectroscopy. in S Fantini & P Taroni (eds), *Optical Tomography and Spectroscopy of Tissue XV.*, 1237606, Proceedings of SPIE. Progress in biomedical optics and imaging, vol. 12376, SPIE, Optical Tomography and Spectroscopy of Tissue XV 2023, San Francisco, United States, 30/01/23. https://doi.org/10.1117/12.2651676

High-speed spatial parameter recovery using multi-distance frequency-domain diffuse optical spectroscopy

Robin Dale[a], Thomas D. O'Sullivan[b], Scott Howard[b], Chris Campbell[b], Felipe Orihuela-Espina[a], and Hamid Dehghani[a]

[a]University of Birmingham, Edgebaston, Birmingham, UK
[b]University of Notre Dame, Indiana, USA

ABSTRACT

Frequency domain (FD) diffuse optical spectroscopy (DOS) can be used to recover absolute optical properties of biological tissue, providing valuable clinical feedback, including in diagnosis and monitoring of breast tumours. In this study, tomographic (3D) and topographic (2D) techniques for spatially-varying optical parameter recovery are presented, based on a multi-distance, handheld DOS probe. Processing pipelines and reconstruction quality are discussed and quantitatively compared, demonstrating the trade-offs between depth sensitivity, optical contrast, and computational speed. Together, the two techniques provide both depth sensitive real-time feedback, and high-resolution 3D reconstruction from a single set of measurements, enabling faster and more accurate clinical feedback.

Keywords: diffuse optical spectroscopy, diffuse optical tomography, topography

1. INTRODUCTION

Near-infrared spectroscopy (NIRS) is a non-invasive medical imaging technique, in which the attenuation of near-infrared (600-1000nm) light, emitted into biological tissue, and measured at the surface at a distance of 5-50mm, is be used to infer optical characteristics of the intervening tissue, relating to chromophore concentrations including hemoglobin, water, and lipids. NIRS has a variety of clinical and research applications including functional neuroimaging,[1] breast tumour characterisation and monitoring,[2] neonatal care,[3] critical care,[4] and sport.[5] In addition to light attenuation at multiple wavelengths, measured with conventional continuous wave (CW) NIRS, frequency domain (FD) NIRS additionally measures the phase shift of an intensity modulated signal, allowing quantitative reconstruction of tissue optical absorption and scattering, and thus as a safe and effective method for characterizing tissue composition and metabolism.[6] Furthermore, the phase component of the FD signal has also been shown to have greater depth sensitivity than amplitude alone, and can produce higher resolution images when used for tomography.[7]

The design of both NIRS probes and scanning protocols is dependent upon trade-offs between imaging speed, depth sensitivity, and signal contrast. Increased source-detector separation (SDS) is known to increase depth sensitivity while decreasing SNR. Increasing the number of overlapping multi-distance measurement channels improves SNR and imaging resolution at the cost of increased instrumental complexity and processing. While FD-NIRS systems have historically been more complex and expensive than CW, resulting in limited clinical impact, recent developments in hardware have greatly reduced these barriers. Stillwell et al. have developed a handheld FD-NIRS platform capable of measuring optical properties and tissue chromophore concentrations in real-time.[8] The device uses a high-speed look-up table and onboard CPU to achieve a maximum sample speed of 36,600Hz for amplitude and phase data at a single wavelength and single modulation frequency, with the capability to sweep through six wavelength and hundreds of modulation frequencies. This device has been demonstrated for high-speed spectroscopy and 2D topography using optical phantoms, showing great potential for providing real-time feedback in clinical settings. A further benefit of the system is scalability; multiple channels can be incorporated in the same hardware paradigm, without reducing the high sampling rate.

Further author information: (Send correspondence to Robin Dale)
Robin Dale: E-mail: rbd079@student.bham.ac.uk, Telephone: +44 7508 399 716

Figure 1. The handheld probe[8] and scanning technique simulated in this study.

This work examines two methods for spatially-varying optical property reconstruction - volumetric tomography using NIRFAST,[9] and multi-distance topography - based on a one-source / three-detector FD probe, and a simple grid-scan protocol that could be applied with the handheld high-speed scanner. The reconstructions produced via these two methods are quantitatively compared, and used to characterise the relationship between source/detector separation, depth sensitivity, and signal contrast, using intensity and phase of the measured signal, at a single modulation frequency.

2. METHODS

2.1 Simulated Data

A 110x110x50mm finite element model (FEM) mesh with 79,490 nodes and 454,320 linear tetrahedral elements, with background properties $\mu_a = 0.01mm^{-1}, \mu_s' = 1mm^{-1}$, was generated using the NIRFAST toolbox. Sources and detectors were placed according to a simple linescan protocol in which the probe, with a single source and three detectors arranged in a line at 10, 20 & 30mm source detector separations (SDS), was moved across the surface of the model at 10mm intervals. This process was repeated with the probe in horizontal and vertical positions. The resulting data for each mesh consisted of 480 individual measurement channels. Realistic system noise was added to the simulated amplitude and phase measurements using a amplitude-dependent noise model derived from real measurements taken on an optical phantom.

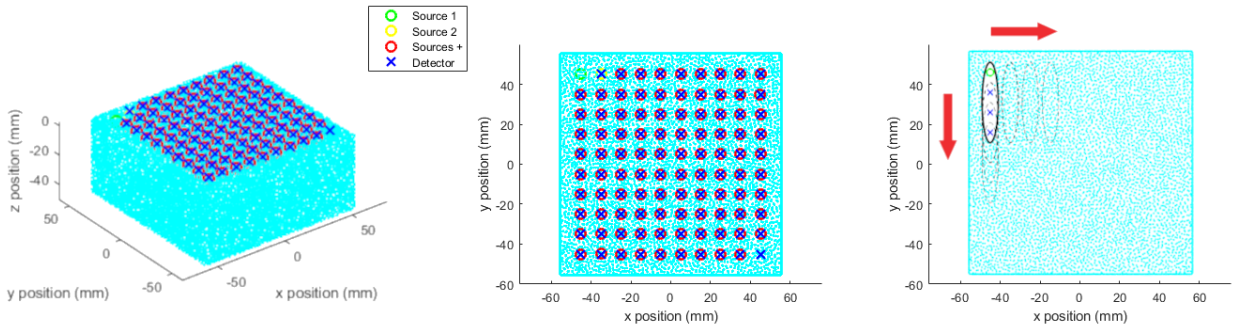

Figure 2. FEM mesh used to simulate FD-NIRS measurements, showing source/detector arrangement and linescan protocol

Three cylindrical inclusions (10mm depth, 10mm radius) were added to simulate independent and conjunctive perturbations of 150% magnitude in μ_a and μ_s'. This process was repeated with the inclusions positioned at

depths between 2.5 - 20mm, at increments of 2.5mm, fig. 4.

2.2 Tomography

A voxelised Jacobian ($J \in \mathbb{R}^{n\_channels \times n\_voxels}$) sensitivity matrix was calculated for 480 channels and 34,990 voxels, using the Adjoint method.[9] By definition, J relates a change of measured data due to a small change in optical properties, which can used to iteratively update absolute maps of μ_a and μ_s' using:

$$[J^T J + \lambda I]\Delta\mu_i = J^T \delta_{i-1} - \lambda I(\mu_{i-1} - \mu_0) \tag{1}$$

where J is the Jacobian, λ is a regularization parameter, I is an identity matrix, $\mu = [\mu_a, \mu_s']$, μ_0 is the initial guess, and i is the iteration number.

2.3 Topography

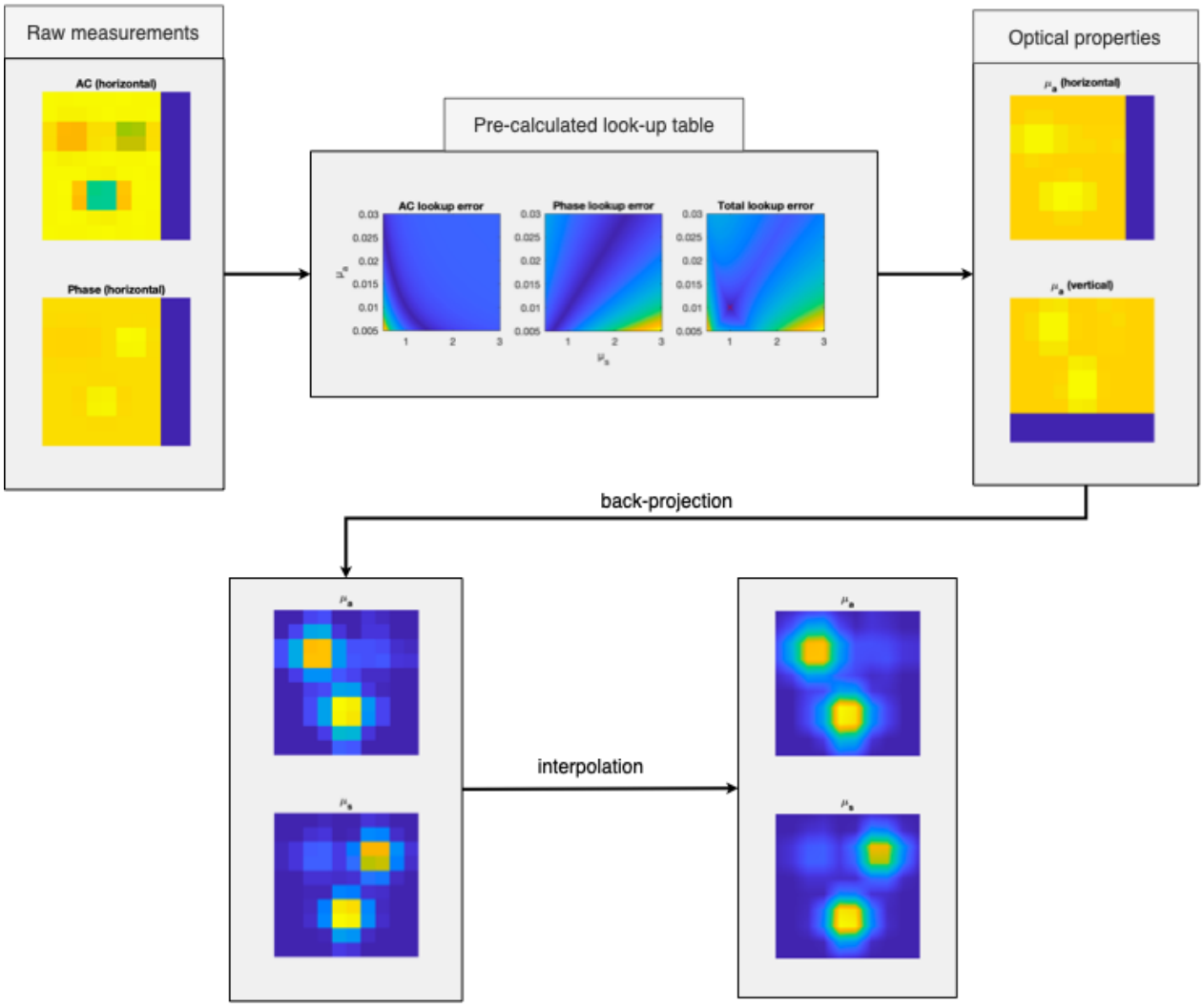

Figure 3. Processing pipeline for topographic reconstruction of μ_a, with SDS of 20mm. The same process is used for μ_s', and for each other SDS.

For 2D topographic reconstruction, the measured amplitude and phase components of the FD signal were separated according to SDS, and arranged according to probe location (fig. 3). To emulate the onboard processing procedure used in[10] , an optical property look-up table was pre-calculated using a semi-infinite forward model of the diffusion equation. μ_a values between $0.005mm^{-1}$ and $0.03mm^{-1}$, at $0.0001mm^{-1}$ increments, and mu'_s values between $0.05mm^{-1}$ and $0.3mm^{-1}$, at $0.001mm^{-1}$ increments, were calculated and stored, producing a 251x251 table for intensity and phase shift for each of the three SDSs of 10, 20, and 30mm. The simulated linescan measurements were calibrated with respect to the semi-infinite analytical model used to generate the lookup table. The table was used for high-speed bulk optical parameter estimation in a voxel-by-voxel manner:

$$\min_{\mu_a,\mu_{s'}} ||Y - T(\mu_a, \mu'_s)||_2 \tag{2}$$

where $Y = \begin{bmatrix} meas^i \\ meas^{ph} \end{bmatrix}$, and $T(\mu_a, \mu'_s) = \begin{bmatrix} lookup^i \\ lookup^{ph} \end{bmatrix}$ for the given μ_a and μ'_s. This produced a set of topographical images for both μ_a and μ'_s, for both vertical and horizontal scans, for each SDS. The vertical and horizontal scan measurements were combined via a simple back projection algorithm: each measurement was associated to each grid-point between the source and detector, inclusively. The values of each point were then calculated as the average of each measurement associated with them. The resulting 10x10 topographical maps were bi-cubically interpolated to produce the final output, shown in fig 6.

3. RESULTS

Figures 5 and 6 show the tomographic and topographic reconstructions based on measurements from the target volume shown in fig. 4, with three inclusions at 10mm depth.

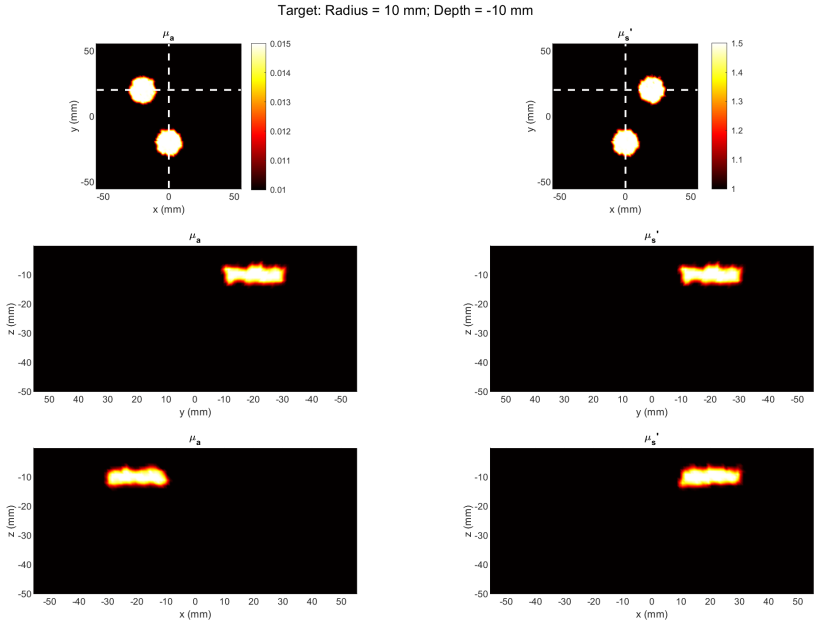

Figure 4. Target μ_a and $\mu_{s'}$ inclusions at 10mm depth. The top row shows a lateral slice at z = -10. The vertical and horizontal dashed lines in the top row indicate the x and y coordinates of the slices in the third rows respectively.

The lateral position and size of the inclusions are accurately reconstructed by tomography up to a depth of 20mm and by topography up to 10mm. Tomography additionally reconstructs the upper and lower boundaries of the inclusions accurately up to 10mm depth. The topographical images have lower resolution due to the course voxelisaton of the measurement space. This effect can be reduced by generalising the procedure to a finer grid

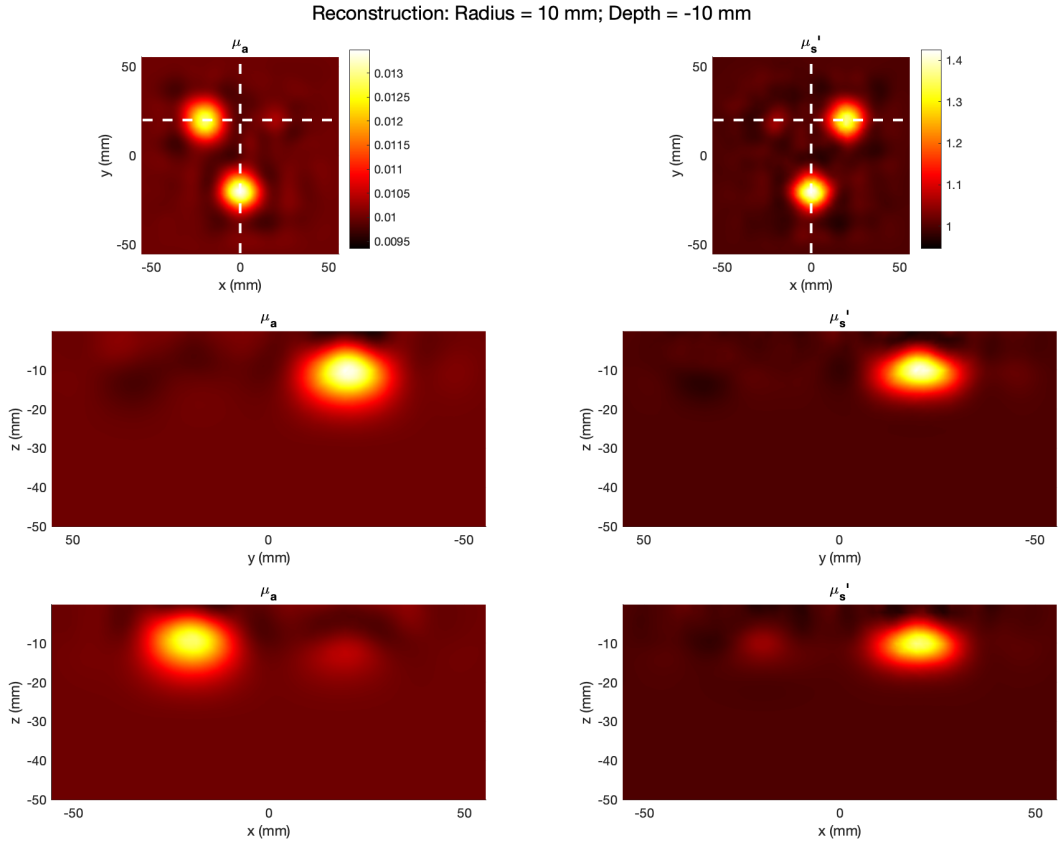

Figure 5. Tomographic reconstruction of target volume from fig. 4, with inclusions at 10mm depth. The top row shows a lateral slice at z = -10. The vertical and horizontal dashed lines in the top row indicate the x and y coordinates of the slices in the third rows respectively.

(as in[10]). The topographic process generates small horizontal and vertical artefacts around the inclusion, due to the heuristic back-projection algorithm, which are not present in the tomographic reconstruction.

Fig. 3.1 shows the sensitivity of tomographic and topographic reconstructions to μ_a and $\mu_{s'}$ perturbations at multiple depths. As anticipated, the max inclusion/background contrast in both μ_a and $\mu_{s'}$ is highest in the 10mm reconstruction, and decreases with increased SDS and inclusion depth, due to lower SNR, and the perturbation volume contributing less to the bulk optical parameter. Tomography consistently provides higher resolution and contrast than topography. The three layers of topographic reconstruction are sensitive to perturbations at different depths, as a function of SDS; shallower inclusions are most visible in the 10mm channel, while deeper inclusions are more visible in 20mm and then 30mm channels. However, the fall-off in contrast as inclusion depth increases occurs earlier for scattering (sharply around 7.5mm) than absorption (gradually between 7.5 and 20mm). At 10mm inclusion depth, absorption is clearly visible in all three SDS channels, while scattering is visible only in second and third nearest neighbours (20 and 30mm SDS). There is some cross-talk between the two optical parameters in both topographical and tomographic reconstructions, however the effect is far greater in the topography above 7.5mm inclusion depth, due to the relatively higher absorption sensitivity.

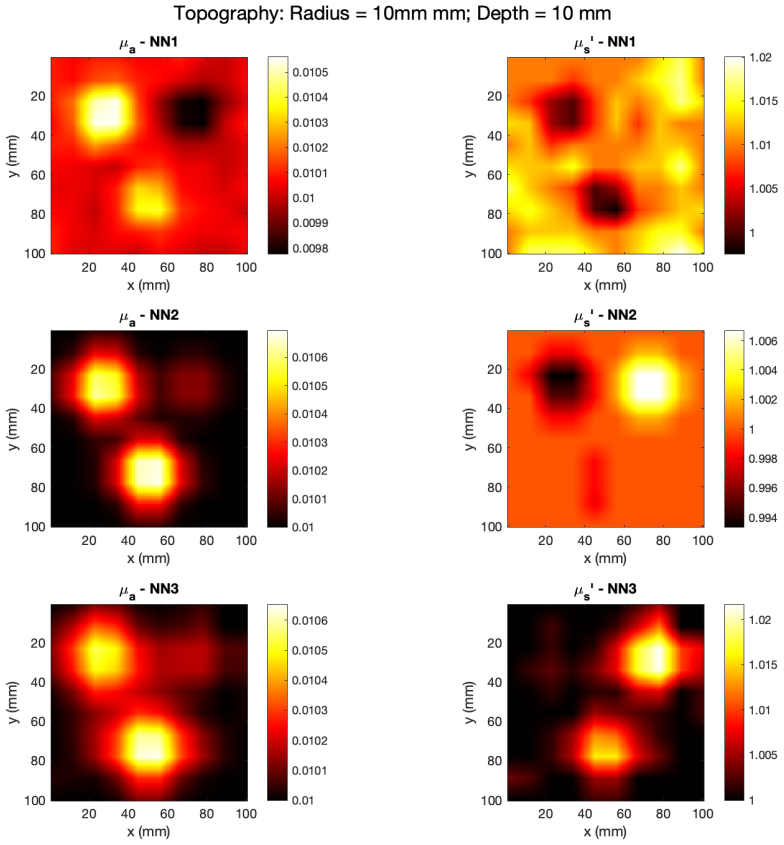

Figure 6. Multi-SDS topographic reconstruction of target volume from fig. 4, with inclusions at 10mm depth. The 3 rows correspond to the three 'Nearest Neighbour' sources: 1=10mm, 2=20mm, 3=30mm

3.1 Computation time

The time taken to compute the reconstructions, as described above, was measured on a Macbook air laptop with 8GB DDR4 RAM and M1 chip. The three-layer topographic reconstruction completed in 0.45 seconds. The tomographic reconstruction took 72 seconds on average per iteration. Total reconstruction time depended on the number of iterations and therefore on the stopping condition. The reconstruction in fig. 5 took 15 iterations and a total of 18 minutes.

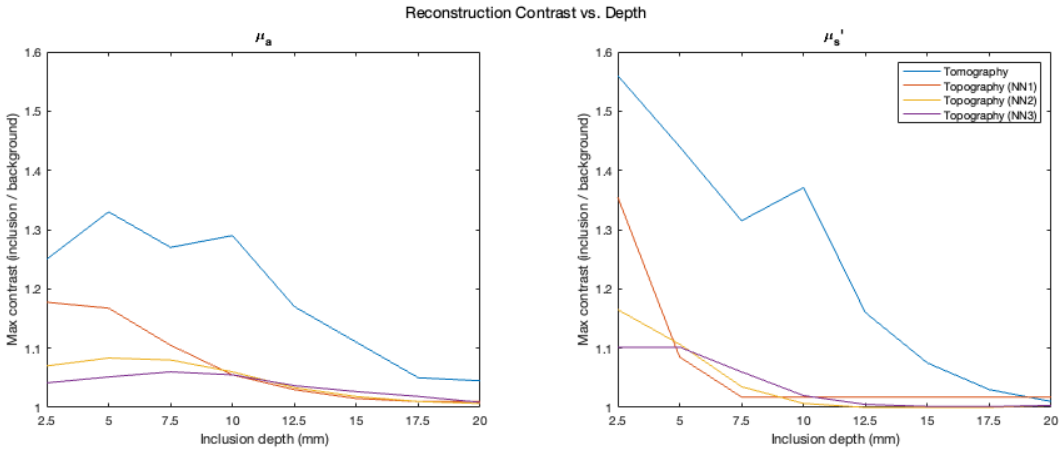

Figure 7. Optical contrast of μ_a and $\mu_{s'}$ reconstructions using tomography and topography with inclusions at multiple depths between 2.5 - 20mm.

4. DISCUSSION

Both topographic and tomographic techniques as described above can accurately reconstruct background values and perturbations in optical absorption and reduced scattering. 3D Tomography Using NIRFAST provides greater resolution, can reconstruct the depth-wise shape of the inclusion in addition to the lateral shape, and has higher contrast for deeper inclusions as compared to topography, and is therefore preferable for offline tissue imaging. Furthermore, tomography is more adaptable to variation in shape and composition of tissue, and therefore a wider range of applications, because the optimisation can be conducted on layered and non-homogenous FEM models, thereby incorporating physiological priors in the reconstruction.

The benefit of the topographic approach is the high speed of computation, which complements the practicality of NIRS in a clinical environment as compared to other imaging modalities. In conjunction with the scalable handheld probe described in[8] this technique facilitates spatially-resolved, depth-sensitive, rea-ltime feedback to the researcher or clinician performing the scan. To enhance the clinical impact of this approach, a focus of future research will be the integration of real-time positional information from a handheld probe alongside spectroscopy data, in order to continuously update the topographic reconstruction. It may be advantageous to thus combine the two approaches, using multi-depth topography as a 'scout-mode', to determine areas of interest which can then be the focus for full tomography, using all, or a subset of the same measurements.

ACKNOWLEDGMENTS

Research reported in this publication was supported by the National Institute of Biomedical Imaging and Bioengineering (NIBIB) of the National Institutes of Health (NIH) Award Number R01EB029595

REFERENCES

[1] Pinti, P., Tachtsidis, I., Hamilton, A., Hirsch, J., Aichelburg, C., Gilbert, S., and Burgess, P. W., "The present and future use of functional near-infrared spectroscopy (fnirs) for cognitive neuroscience," *Annals of the New York Academy of Sciences* **1464**(1), 5 (2020).

[2] O'Sullivan, T. D., Leproux, A., Chen, J.-H., Bahri, S., Matlock, A., Roblyer, D., McLaren, C. E., Chen, W.-P., Cerussi, A. E., Su, M.-Y., et al., "Optical imaging correlates with magnetic resonance imaging breast density and reveals composition changes during neoadjuvant chemotherapy," *Breast Cancer Research* **15**(1), 1–15 (2013).

[3] Sood, B. G., McLaughlin, K., and Cortez, J., "Near-infrared spectroscopy: applications in neonates," in [*Seminars in Fetal and Neonatal Medicine*], **20**(3), 164–172, Elsevier (2015).

[4] Pham, T. H., Hornung, R., Ha, H. P., Burney, T., Serna, D., Powell, L., Brenner, M., and Tromberg, B. J., "Non-invasive monitoring of hemodynamic stress using quantitative near-infrared frequency-domain photon migration spectroscopy," *Journal of biomedical optics* **7**(1), 34–44 (2002).

[5] Hamaoka, T., McCully, K. K., Niwayama, M., and Chance, B., "The use of muscle near-infrared spectroscopy in sport, health and medical sciences: recent developments," *Philosophical Transactions of the Royal Society A: Mathematical, Physical and Engineering Sciences* **369**(1955), 4591–4604 (2011).

[6] O'Sullivan, T. D., Cerussi, A. E., Tromberg, B. J., and Cuccia, D. J., "Diffuse optical imaging using spatially and temporally modulated light," *Journal of biomedical optics* **17**(7), 071311 (2012).

[7] Doulgerakis, M., Eggebrecht, A. T., and Dehghani, H., "High-density functional diffuse optical tomography based on frequency-domain measurements improves image quality and spatial resolution," *Neurophotonics* **6**(3), 035007 (2019).

[8] Stillwell, R. A. and O'Sullivan, T. D., "A real-time fully handheld frequency domain near infrared spectroscopy imaging system," in [*Multiscale Imaging and Spectroscopy III*], PC119440D, SPIE (2022).

[9] Dehghani, H., Eames, M. E., Yalavarthy, P. K., Davis, S. C., Srinivasan, S., Carpenter, C. M., Pogue, B. W., and Paulsen, K. D., "Near infrared optical tomography using nirfast: Algorithm for numerical model and image reconstruction," *Communications in numerical methods in engineering* **25**(6), 711–732 (2009).

[10] Stillwell, R. A., Kitsmiller, V. J., Wei, A. Y., Chong, A., Senn, L., and O'Sullivan, T. D., "A scalable, multi-wavelength, broad bandwidth frequency-domain near-infrared spectroscopy platform for real-time quantitative tissue optical imaging," *Biomedical optics express* **12**(11), 7261–7279 (2021).